DEVELOPMENT AND EVALUATION OF A VTOL OBSERVATION PLATFORM

F. Buysschaert*, M. Yacoubi*, A. Alami*, E. Kagambage†, G. Dimitriadis†, P. Hendrick*
***Université Libre de Bruxelles, Aero-Thermo-Mechanics Department, F.D. Roosevelt Avenue 50, 1050 Brussels, Belgium**
†Université de Liège, Aerospace and Mechanics Department, Chemin des Chevreuils 1, 4000 Liège, Belgium

Keywords: *UAV, Duct, Rotor, Performance*

Abstract

An aerodynamic study of the ULB-developed ducted rotor MAV using the results of full-scale wind tunnel tests allowed the determination of the platform's positive speed envelope, power requirements and endurance characteristics for ISA sea level conditions. In this study, the power consumption appears to be majorly depending on the rotor rotational speed, while an increase in horizontal speed results in a duct operating more as a circular wing, also unveiling a power bucket as is the case with conventional helicopters. A positive influence of the ground proximity on the total thrust has been monitored.

1 Introduction

A couple of decades ago, few amongst us would have believed that what was once a buzzing contraption made by amateurs for leisure purposes terrorizing the Sunday skies has now become the target of profound research and a key element in the contemporary battlefield intelligence. What began with flying remotely controlled aircraft closely around the aerodrome now evolved to Unmanned Aerial Systems (UAS) cruising autonomously towards targets of interest miles away from the base station using satellites as a communication relay. The Unmanned Aerial Vehicles (UAVs) exist in various sizes. One of the most interesting niches concerns the UAVs of moderate size (< 1m), also called Micro Air Vehicles (MAVs). Since the design costs and weight are relatively low, these platforms offer an excellent breeding ground to design and develop new and sometimes exotic concepts, answering to many and mostly military driven requirements. In pursuit of the latest 'Minidrones' competition issued by the French Aerospace Lab ONERA, the Université Libre de Bruxelles decided to continue the development and optimization of the ducted rotor MAV (Fig.1), which was built for this competition and for which Vertical Take-off and Landing (VTOL) capabilities and autonomous flight were mandatory.
Although the MAV appears familiar to other ducted-rotor concepts such as iStar [1], Cypher [2], Hovereye [3], it fundamentally differs from

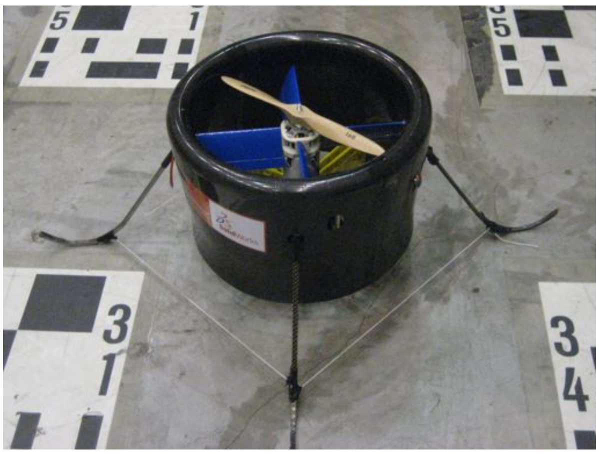

Fig. 1 The ULB-MAV

these platforms while it uses the downwash of a single rotor to compensate motor torque and achieve control around roll, pitch and yaw axes. This is obtained by means of variable camber and incidence blades, installed inside the duct and downstream the rotor. The subsequent paragraphs will expound the component layout of the MAV, the aerodynamic characteristics obtained from full-scale wind tunnel tests and an important part of the performance envelope.

2 Concept survey

2.1 MAV general layout

Fig. 2 shows a cutaway of the MAV unveiling its major components. The rotor is mounted on a permanent magnet brushless motor fixed in a solid ABS housing made via rapid prototyping. On this block, the flight control systems and payload are mounted as well as the protective carbon fibre shell, which forms the centre fuselage. Duct suspension rods join the centre fuselage and the duct. In the duct, each suspension rod is bolted in an ABS housing. These housings, four in total, are clamped between two carbon fibre reinforced plastic rings. The rings assure structural rigidity while offering in between sufficient space to install the, in proportion to the MAV weight, heavy Lithium-Polymer batteries. A carbon fibre reinforced plastic skirt shapes the duct and is fixed on ribs having the requested duct aerodynamic profile. Table 1 reviews some of the most important components in the MAV. Note that most components are off-the-shelf components in order to reduce development cost and time.

2.2 Flight controls

Directional control is achieved by variable camber blades of which the primary function is the compensation of motor torque (Fig. 4). These 'anti-torque' blades are installed in the duct at a predetermined angle δ with respect to the vertical axis of symmetry, producing a lift force and thus torque commensurate with rotor rotational speed Ω, as can be derived from Fig. 3. There one observes the angle of incidence γ_r increase monotonically with Ω. γ_r is by definition the angle between the airflow velocity vector near the anti-torque blades and the vertical axis of symmetry of the UAV, from which follows :

$$\alpha_r = \gamma_r - \delta \tag{1}$$

where α_r the anti-torque blade angle of attack. But besides a higher α_r, an increasing rotor speed results in more rotor thrust too and thus causes a higher downwash velocity with magnitude v_i which also contributes to a sensible raise in anti-torque. Thanks to a servomotor-controlled trailing edge flap, sufficient anti-torque and yaw control margin remains available.

Lateral and longitudinal control is provided

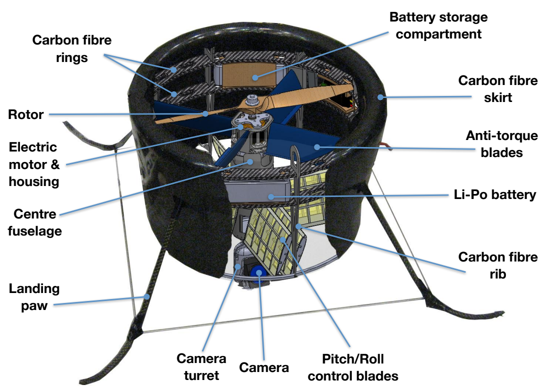

Fig. 2 ULB-MAV Cutaway view.

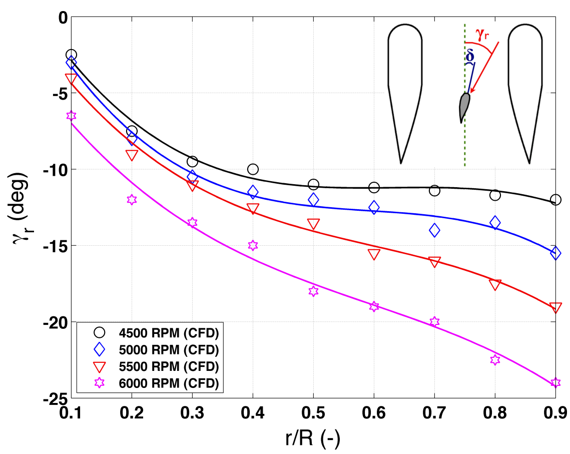

Fig. 3 Impact of rotor speed on airflow angle of incidence γ_r near the anti-torque blades [4][5].

Table 1 Principal element overview.

Element	Parameter	
Propulsion system		
Brushless motor : Scorpion S4020-12	Continuous power	1800 (W)
Propeller (rotor) : Menz 16/8 (modified)	Diameter	0.40 (m)
Batteries : Thunder Power TP3850-3SXV	Capacity	15.4 (Ah)
Structure : dimensions		
Duct	Diameter	0.40 (m)
	Chord	0.30 (m)
	Thickness-to-chord ratio	0.15 (-)
Centre fuselage	Diameter	0.08 (m)

by the 'pitch and roll' control blades installed below the anti-torque blades. Four 'biplane' control blades are used for this purpose (Figs. 2 and 5). This configuration eases the flight control algorithms by avoiding cross-coupling effects between pitch and roll, while the biplane configuration confines the duct length to a strict minimum (Fig. 2). The blades have variable angle of incidence and are directly positioned by servomotors installed in the centre fuselage.

2.3 Mass

The mass of the MAV has a significant impact on the platform's power requirements and performance [6]. Therefore, the mass of the MAV has been minimized using composite materials and plastics for the larger structural components, installing a brushless permanent magnet motor exhibiting a high mass-weighed power density and profiting from the high energy and power density of lithium polymer batteries. A survey of the mass of the major systems present in the MAV is shown in Fig. 6. During early tests, no structural instabilities were observed [7]. The total mass amounts to 3.5 kg, including the payload.

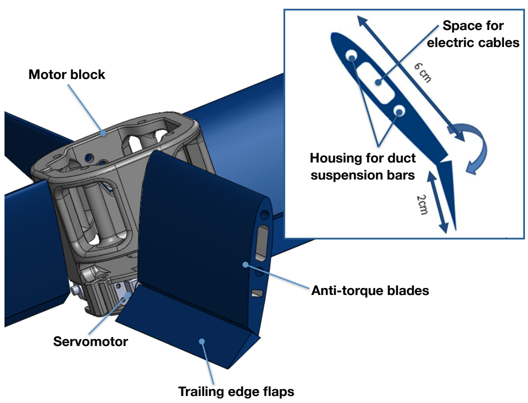

Fig. 4 Anti-torque blades with movable trailing edge flaps.

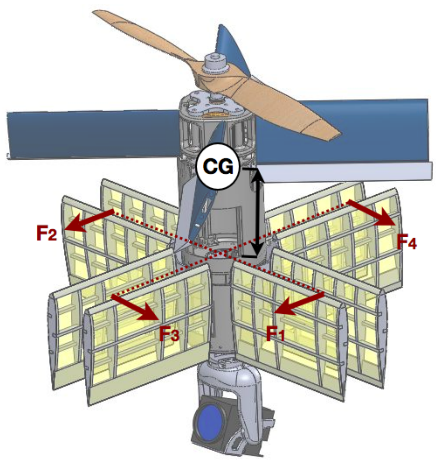

Fig. 5 Decoupling of pitch and roll axes by smart positioning of control blades (CG=centre of gravity).

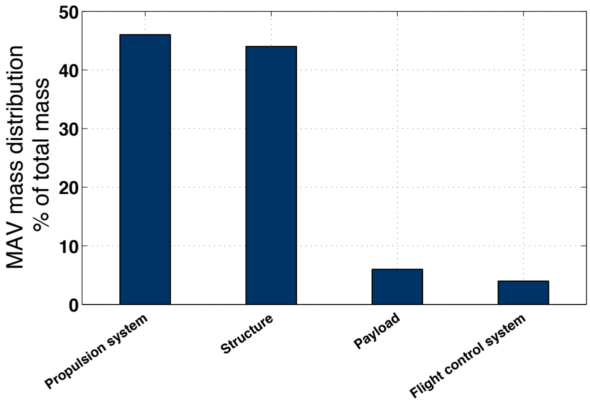

Fig. 6 Major system mass survey.

Fig. 7 Full-scale wind tunnel tests in the subsonic wind tunnel of the Liège University, Belgium.

3 Performance

3.1 Aerodynamics

3.1.1 Wind tunnel test set-up

The aerodynamic performance of the MAV was tested full-scale in the subsonic wind tunnel of the University of Liège, Belgium, for various angles of attack, rotor rotational speeds and airspeeds. The vertical axis of symmetry (X-axis on Fig.14) of the MAV was placed in the earth horizontal plane and mounted on an arm with force and torque sensors (Fig. 7). One obtained a variation of the MAV angle of attack α by rotating the arm around its vertical axis. The rotor rotational speed was set manually via a radio transmitter and recorded optically. The anti-torque blades could not be removed for structural reasons and were given a fixed angle of incidence. No control blades were installed. An elaborate test campaign allowed determining the aerodynamic forces and moments around the MAV aerodynamic (lift-drag) and body-reference frames, as elucidated in Fig. 14. The origin of both coordinate systems were set in the plane tangent to the leading edge of the rotor duct ($x_{LE} = 0$, $x_{ae} = 0$).

3.1.2 Wind tunnel test results and analysis

Figures 8-11 show the lift $L-$ and drag $D-$forces as well as the pitching moment M_Y around the duct leading edge for an angle of attack range α from 0° to 180°, with a varying airspeed of the airflow far upstream the rotorcraft V_∞ of 0, 5, 12 and 15 m/s and several rotor rotational speeds, i.e. 0, 3000, 5000 and 8300 RPM. Since during the wind tunnel tests no means were available to identify the total thrust produced by rotor and duct separately, this force will be inherently present in the lift and or drag forces, with its impact on the latter two forces depending on the angle of attack α. The sign convention used is the one indicated in Fig. 14. The data in Figures 8-11 show significant fluctuations, of which the origin was esteemed to be caused by the fluctuating systematic errors from the data acquisition system clearly observed during the measurements. Future tests will therefore use a more tailored and robust data acquisition system. For this paper, the data was slightly modified by removing inconsistencies due to the above mentioned errors in order to represent physically acceptable values for an axisymmetric aircraft.

For $V_\infty = 0$ m/s (Fig. 8), the angle of attack α has no real significance, though it represents a varying position of the V_∞-vector in a static environment, even though its magnitude is zero. Since the thrust is here a pure function of rotor rotational speed and its direction aligned with the X-axis of the aircraft, one obtains the lift and drag evolution with angle of attack shown in Fig. 8 by simply transforming the thrust force vector in the body reference frame to the lift-drag coordinate

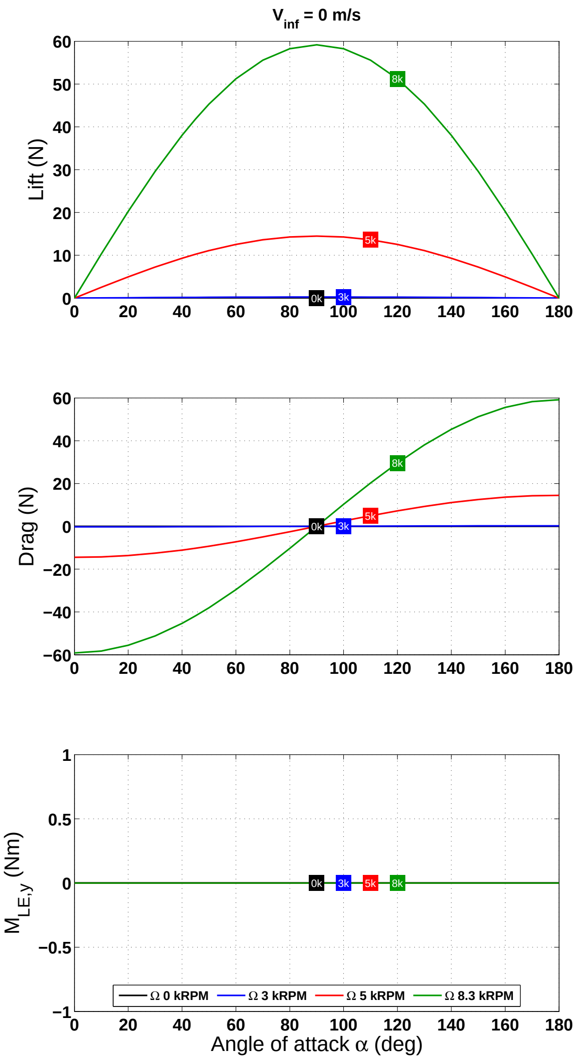

Fig. 8 $V_\infty = 0$ m/s, ISA SLS

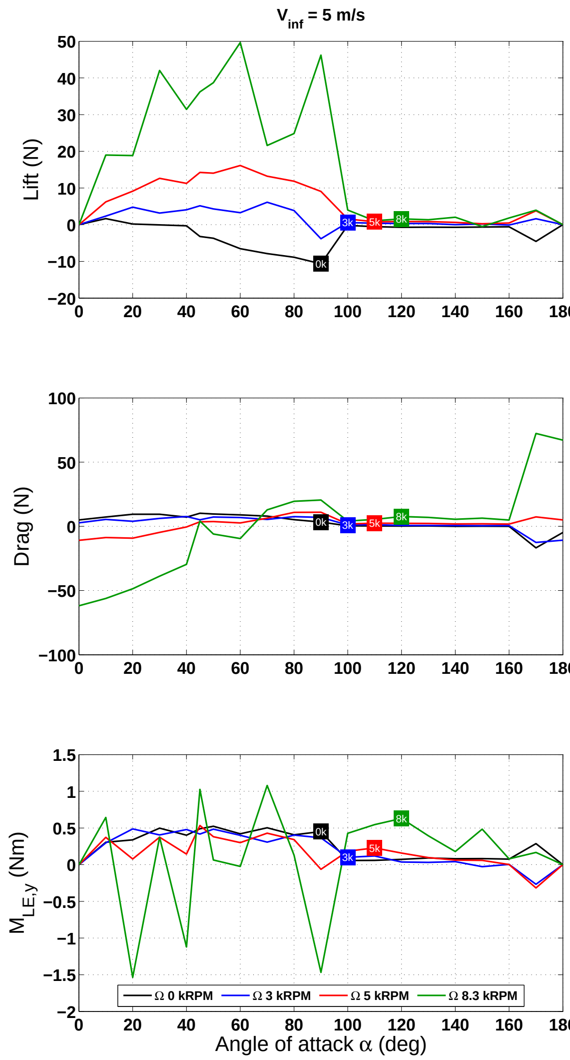

Fig. 9 $V_\infty = 5$ m/s, ISA SLS

system. The thrust becomes of importance above 5000 RPM. Due to the aircraft's symmetry, the pitching moment M_Y around the Y-axis remains zero.

For non-zero free stream velocities V_∞, the drag is mostly related to the thrust in the first half of the first α-quadrant Q_0^{45} (α=0...45°), while the lift force becomes more depending on the thrust in the second half of the first α-quadrant Q_{45}^{90}. Indeed, in Q_0^{45}, the drag is mostly negative for the higher range of rotor rotational speeds, say above 5000 RPM. However, for V_∞ around 12 m/s, the drag becomes positive for small angles of attack (α below 10 °). This phenomenon could be explained by the fact that a fixed pitch propeller is used. Indeed, the used propeller has relatively low angles of attack near the tip (washout) while there, most of the thrust is produced. Increasing V_∞ beyond a certain level will cause the average angle of attack α_R of the propeller blades to become negative, resulting in a reversal of the thrust direction. Interestingly, this problem disappears quickly when α passes 10°. A similar behaviour is recorded for lower V_∞ at lower ro-

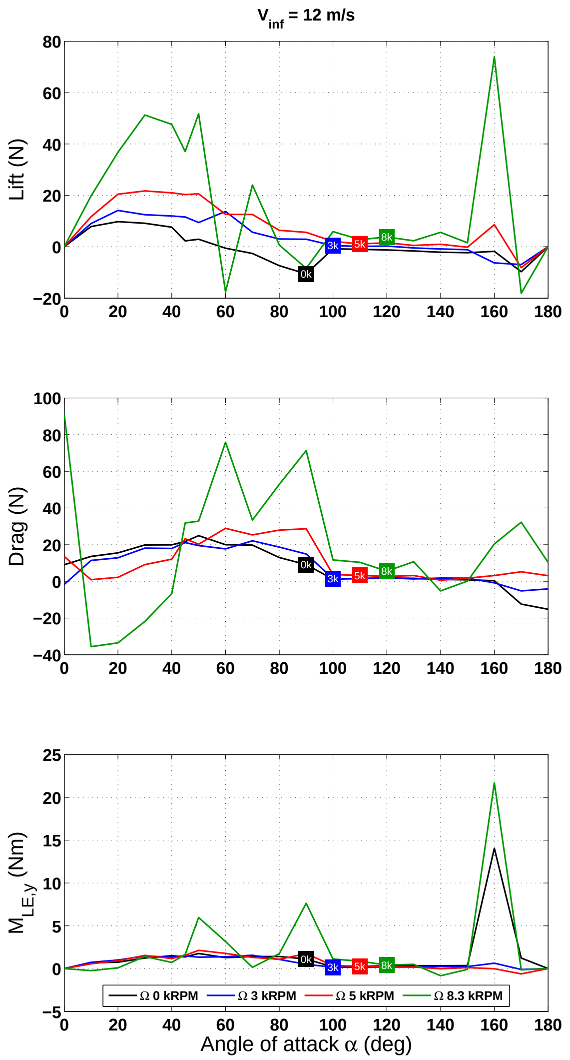

Fig. 10 V_∞ = 12 m/s, ISA SLS

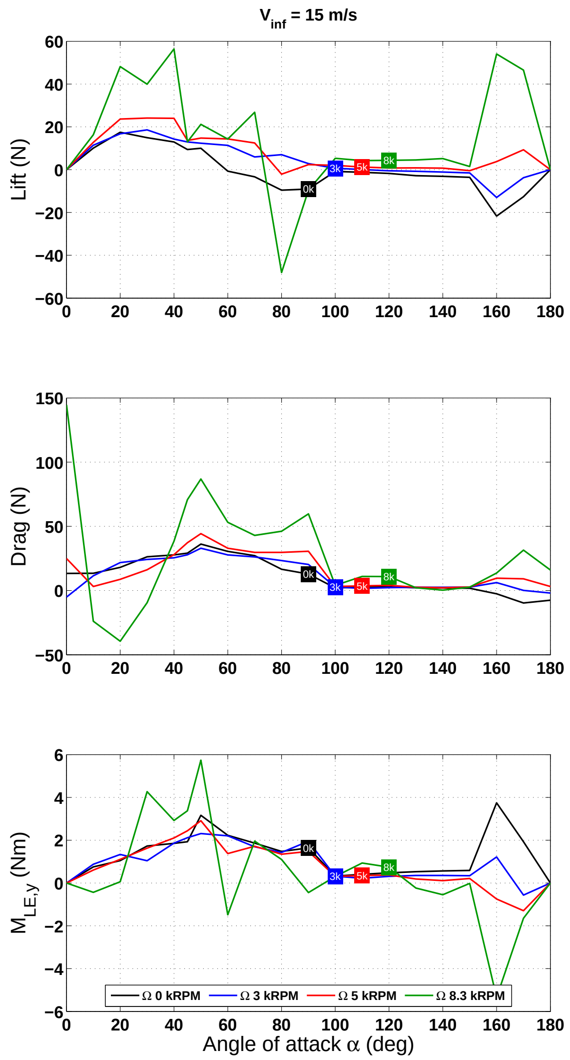

Fig. 11 V_∞ = 15 m/s, ISA SLS

tor rotational speeds. For the second half of the second quadrant Q_{135}^{180}, a positive drag represents thrust, though the operating conditions for the rotor are different. Indeed, the downwash of the rotor has to work against the dynamic pressure of the free stream flow. Once the dynamic pressure of the free stream becomes larger than the dynamic pressure near the duct exit, the flow reverses completely. This is the case for the higher V_∞ where the slower turning rotor regimes get faster into stall and will no longer produce thrust but drag instead. For Q_{45}^{90} and Q_{90}^{135} and for V_∞ higher than 5 m/s, the drag is generally positive and exhibits a maximum near $\alpha = 80°$.

An important operating region is the horizontal translation of the aircraft with pitch angles θ (Fig. 14) near 90° as it represents the departing point from hover to horizontal flight. There, the angle of attack α approaches 90°. One observes the lift to drop rapidly with increasing V_∞. For V_∞ near 15 m/s, the lift even becomes negative. Also, around $\alpha = 90°$, it is difficult to explain the various observed lift tendencies. Therefore new wind tunnel tests should map this area more carefully, with a more suited acquisition system.

Finally, one could hardly speak about consistent pitching moments M_Y. For Q_0^{90}, over the complete V_∞ speed range, one may generally expect a positive, nose up pitching moment, as will be shown by the results discussed in paragraph 3.2. Again, new wind tunnel tests will be mandatory.

3.1.3 Ground effect

When on the ground, the MAV rests on its landing structure with the ground surface relatively close to the duct trailing edge plane. The ground proximity effect on thrust should therefore be examined, since it can have a blocking effect on the airstream through the duct. During the wind tunnel test campaign, the ground was simulated with a plate mounted at several distances from the duct trailing edge plane. Fig. 12 surveys the thrust evolution for two rotor rotational speeds, viz. 3000 and 6000 RPM. For both rotational speeds, one observes similar thrust tendencies when moving the plate backwards. Initially the thrust decreases to a minimum near 0.2 m, after which it increases to a maximum at 0.3 m. Moving the plate further away causes the thrust to decline again, though now permanently, towards the unperturbed thrust setting, i.e. without ground in the surroundings. Probably, the first drop in thrust is caused by a reduction of the pressure build-up between rotor and duct exit plane. Though, while moving further away from the ground, the air mass flow through the duct increases due to a reduced blocking effect causing a rise of thrust. After 0.3 m, the positive effect of ground proximity is further degraded, as seen also with conventional, non-ducted rotorcraft [8]. Future wind tunnel tests with pressure sensors placed inside the duct at various positions are planned and will help to further analyse and better understand the observed phenomena.

3.2 Performance assessment

In this paragraph, some important performance characteristics will be expounded. For this purpose, one must first determine the flight conditions where flight in equilibrium can be obtained. This paper only discusses the longitudinal equilibrium.

3.2.1 Longitudinal equilibrium calculation

Five variables -for a given altitude- influence the longitudinal equilibrium and corresponding flight regime of the aircraft, viz. the rotor rotational speed Ω, the MAV pitch angle θ, the climb angle γ, the airflow speed at infinity V_∞ and the angle of incidence of the control blades θ_C (Figs. 13-14). Since for equilibrium,

$$\sum F_X(V_\infty, \theta, \gamma, \Omega, \theta_C) = 0 \tag{2}$$

$$\sum F_Z(V_\infty, \theta, \gamma, \Omega, \theta_C) = 0 \tag{3}$$

$$\sum M_Y(V_\infty, \theta, \gamma, \Omega, \theta_C) = 0 \tag{4}$$

only two variables remain independent. Two variables, Ω and θ_C, can be directly manipulated by the controller and thus set an unambiguous equilibrium state.

As the control blades were absent during the wind tunnel tests, their effect had to be introduced separately. This was done using C_L and C_D characteristics determined via Xfoil. The speed of the airflow over the control blades V_C (Fig. 13) was estimated using the method given in [9] because during the wind tunnel test campaign, no acceptable airspeed measurements near

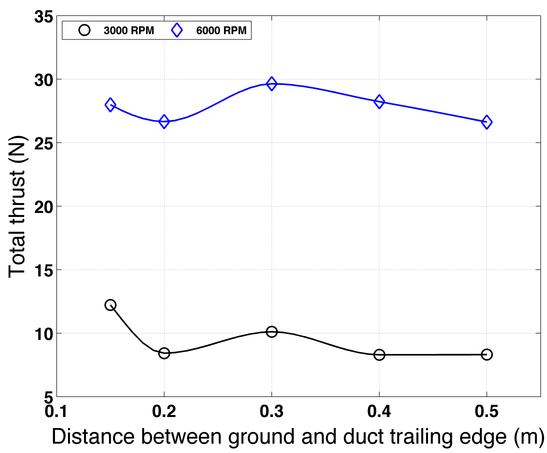

Fig. 12 Effect of ground proximity on total thrust.

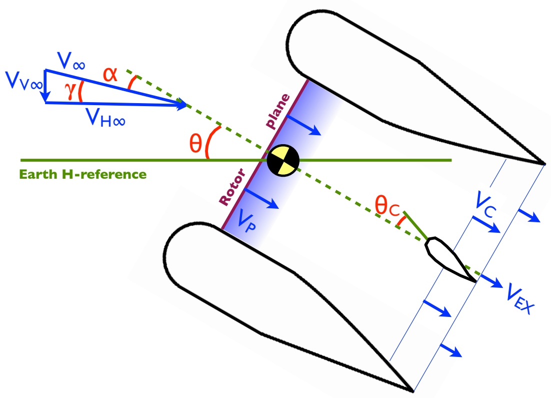

Fig. 13 Velocity field with angle definitions and earth reference frame.

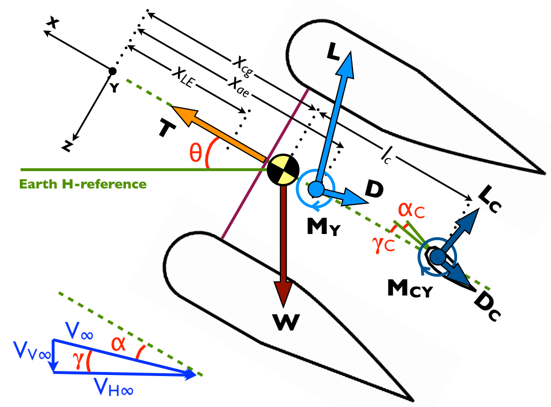

Fig. 14 Representation of forces and moments, angles and definition of body coordinate system (XYZ) with major dimensions.

the duct exit plane (V_{EX}) could be established. Unfortunately, the method uses the momentum theory of which its applicability is limited to a uniform, well developed flow through the duct. According to the CFD-simulations made by [4], the flow in and around the duct during descent can be highly non-uniform, while some wind tunnel tests confirmed the existence of full flow reversal through the duct, but with difficulties to achieve a stable rotor rotational speed, which may also be an indication for a noticeable non-uniform flow. Because of this, only positive climb angles were examined hereby assuming the approximation using the momentum theory to remain acceptable. The study of the airflow velocity distribution in the duct exit plane and a better understanding of the flow direction reversal point and its behaviour throughout the flight envelope will be the subject of future wind tunnel tests using particle image velocimetry (PIV). Another simplification is setting γ_C to zero, which is sensible if one considers the anti-torque blades to have redirected the rather large angle γ_r towards a small value.

3.2.2 Speed envelope

For ISA SLS, the $V_{H\infty}$-$V_{V\infty}$ (defined in Fig. 14) speed envelope was established (Fig. 15) for flight in equilibrium using the aerodynamic data discussed in paragraph 3.1.2. Three regions are indicated on the graph. The effective flight envelope is delimited by the orange line. Outside this area, no possibility exists for equilibrated flight. The second region, indicated by the dark gray zone, covers the results with questionable accuracy. One believes the cause to originate from the scattered aerodynamic data near $\alpha = 90°$. Therefore, the results should be discarded. The third region in light gray contains a speed domain wherein no solutions were found by the solver. The horizontal speed envelope indicated on Fig. 16, which was determined via interpolation, should therefore be handled with care. Here, only more computing time and power with better aerodynamic data can bring the decisive answer.

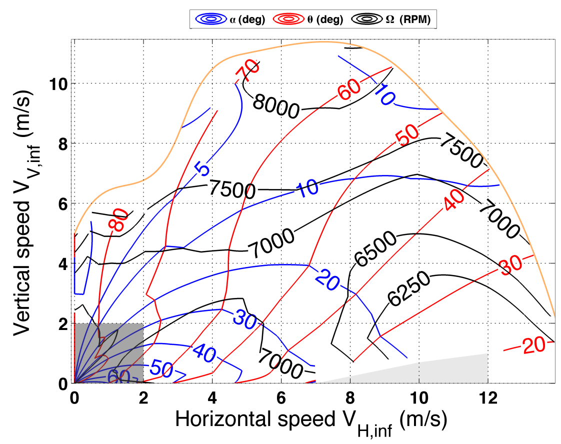

Fig. 15 $V_{H\infty}$-$V_{V\infty}$ speed envelope, ISA SLS.

One learns from Fig. 15 that an increase in horizontal speed $V_{H\infty}$ is obtained by decreasing the pitch angle θ. By so doing, the required rotational speed can be lowered, thus also the thrust setting. Indeed, the duct works more as a circular wing, which offers a higher lift-to-drag ratio. Though, this positive effect disappears for still higher flight speeds, where the drag becomes more important and more thrust must be produced by the rotor. The maximum horizontal speed $V_{H\infty,max}$ was estimated via extrapolation and equals approximately 18 m/s. The highest climb speeds $V_{V\infty,max}$ are achieved at moderate horizontal speeds $V_{H\infty}$ and go up to 10.5 m/s, while during pure climb ($V_{H\infty}$ = 0 m/s), $V_{V\infty,max}$ approaches 6 m/s. Fig. 16 indeed proves the existence of a power bucket as is the case with conventional helicopters.

The required control blade angle θ_C is reflected in Fig. 17. θ_C seems to increase commensurate with $V_{H\infty}$ and inversely proportional to $V_{V\infty}$. The inverse proportionality can be explained by the fact that an increase of $V_{V\infty}$ demands lower angles of attack α causing a raise in mass flow through the duct, but also increased rotor rotational speeds, and thus higher air velocities over the control blades. The impact of the rotor thrust shows to be important, since an increase of horizontal speed exhibits a reduction of θ_C to achieve equilibrium. Nevertheless, the impact of the positive aerodynamic pitching moment should not be discarded. It becomes more important with an increase of V_∞ and the maximum angle of attack of the control blades $\alpha_{C,max}$ is rather low (+/- 10°) under the ruling Reynolds numbers. Higher V_∞ will undoubtedly require larger or more control blades.

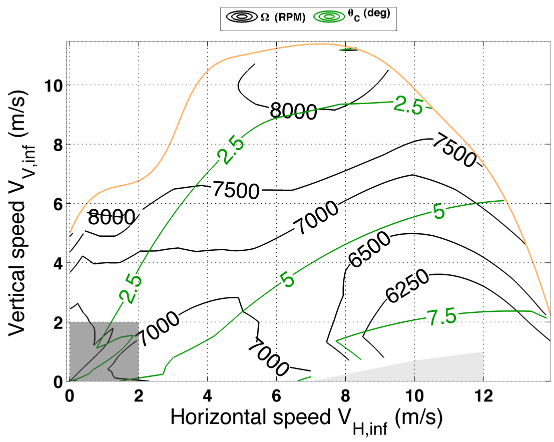

Fig. 17 $V_{H\infty}$-$V_{V\infty}$ speed envelope, ISA SLS, required control blade deflection θ_C.

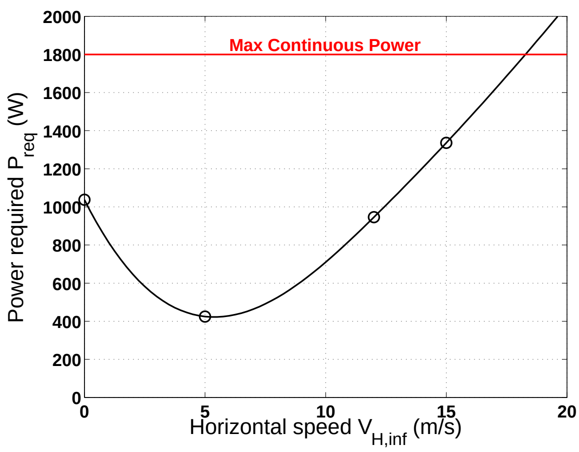

Fig. 16 Horizontal speed envelope at 1000 ft, ISA+7°C.

3.2.3 *Power consumption and endurance*

During the wind tunnel tests, one monitored the electric power consumption to depend almost solely on rotor rotational speed (Fig. 18). Hence, this allows an estimation of the MAV endurance at ISA SLS (Fig. 19), using the results of Fig. 15. From this result, the feasibility of a certain flight profile can then further be examined.

4 Conclusions

From full-scale wind tunnel tests, one recorded the aerodynamic forces and moments of a ducted rotor MAV and this for several free stream wind speed magnitudes and angles of attack. Although the measurements were affected by varying systematic errors, post-treatment still allowed establishing reasonable speed, power and endurance envelopes. Nevertheless, future wind tunnel tests will be required using a more suited acquisition system, which will remove some doubtful results

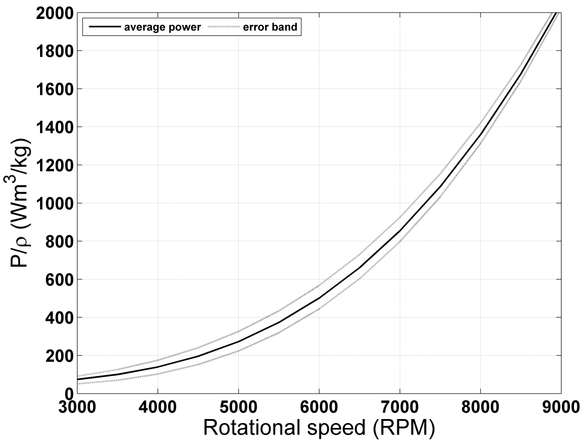

Fig. 18 Evolution of air-density-reduced electric power requirement with rotor rotational speed.

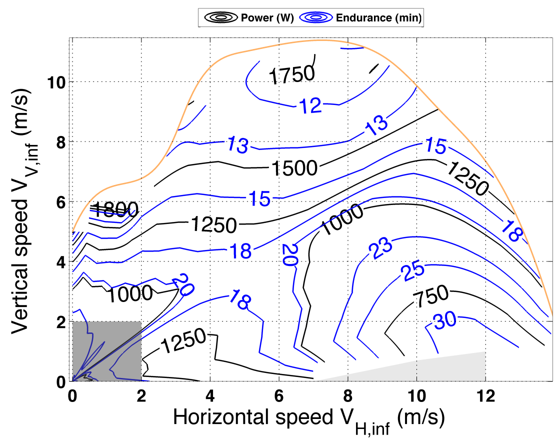

Fig. 19 Electric power consumption and endurance, ISA SLS.

as seen near angles of attack of 90°, for example present during slow horizontal translation. The measurement of the speed of the air exiting/entering the duct near the exit plane will also be paramount because it defines directly the control blade operating conditions, currently limited by modeling to positive vertical speeds. Also, it would be interesting to develop a rotor with variable pitch instead of using an off-the-shelf propeller as it would continue to produce thrust at the higher free stream velocities, where now, it stalls or produces negative thrust. Another, maybe more pragmatic and simple solution would be the installation of a higher voltage battery pack, enabling higher rotational speeds, but this needs more careful examination (engine power limits). Ground proximity showed to have a positive impact on the hover thrust production. Finally, PIV measurements become necessary for further optimisation of the control blades and complete assessment of the flight envelope.

Copyright Statement

The authors confirm that they, and/or their company or organization, hold copyright on all of the original material included in this paper. The authors also confirm that they have obtained permission, from the copyright holder of any third party material included in this paper, to publish it as part of their paper. The authors confirm that they give permission, or have obtained permission from the copyright holder of this paper, for the publication and distribution of this paper as part of the ICAS2010 proceedings or as individual off-prints from the proceedings.

References

[1] Allied Aerospace. *iStar unmanned air vehicles* brochure. 2009.

[2] Antony Angrand. *Cypher de Sikorsky*. Air et Cosmos 1818, page 20, November 16th, 2001.

[3] Bertin Technologies. *Drone miniature à décollage vertical* brochure. 2009.

[4] Jérôme Sans. *Conception et réalisation d'un mini-drone à décollage vertical*. Master's thesis, Université Libre de Bruxelles, Belgium, 2009.

[5] Frank Buysschaert, Moaad Yacoubi, Jérôme Sans, Patrick Hendrick. *Design and assessment of a small autonomous airborne observation platform*. 3rd European Conference for Aero-Space Sciences, July 6-9, 2009, Versailles, France.

[6] Jean-François Aernouts. *Conception et développement d'un mini-drone de type hélicoptère*. Master's thesis, Université de Liège, Belgium, 2005.

[7] Moaad Yacoubi. *Conception et réalisation d'un mini-drone à décollage vertical*. Master's thesis, Université Libre de Bruxelles, Belgium, 2009.

[8] Ray Prouty. *Helicopter performance, stability and control*. Krieger, 2002.

[9] R.I. Lewis. *Turbomachinery performance analysis*. Elsevier Ltd., 1996.